Soil Dynamics and Earthquake Engineering 153 (2022) 107088

Contents lists available at ScienceDirect

Soil Dynamics and Earthquake Engineering

journal homepage: www.elsevier.com/locate/soildyn

Numerical modelling of rammed aggregate piers (RAP) in liquefiable soil

T.S. Thum [a], A. Yerro [a,*], A. Saade [b], E. Ye [c], K.J. Wissmann [d], R.A. Green [a]

[a] Department of Civil and Environmental Engineering, Virginia Tech, United States
[b] Gannett Flemming, United States
[c] Langan, United States
[d] Geopier Foundation Company, United States

ARTICLE INFO

Keywords:
Soil liquefaction
Ground improvement
Rammed aggregate piers
Full-scale field test
Ata
Model calibration
Finite differences
Hydro-mechanical coupling

ABSTRACT

Liquefaction poses a significant risk to the built environment, and as a result, ground improvement (GI) techniques are commonly used to mitigate this risk. Liquefaction mitigation strategies continually evolve, and several relatively new techniques, such as Rammed Aggregate Piers® (RAP), have shown promise. While the densification mechanism associated with many of the GI techniques is generally well known, other mechanisms such as reinforcement, lateral stress increase, and improved drainage that are thought to enhance liquefaction mitigation are still not completely understood. Moreover, field performance data for these GI schemes during actual earthquakes is limited. To fill this gap and evaluate the performance of RAP, this study presents the first numerical model on a specific GI technique that uses detailed site characterization, large-scale field test data, and post-earthquake field performance observations to calibrate and qualitatively validate the model. The in-situ characterization and full-scale field test data collected from the Ground Improvement Programme (GIP) performed following the 2010–2011 Canterbury Earthquake Sequence (CES) in New Zealand are used in this study. A set of fully-coupled hydro-mechanical finite difference (FD) models are performed in natural and reinforced conditions. For the unimproved soil profile, the results predict shear strains and zones of high excess pore water pressures reasonably well. For the profile reinforced with RAP, the analyses indicate that the stiffness properties of the RAP have the greatest influence on the reduction of generated shear strains in the soil profile. Finally, the calibrated models are subjected to a set of ground motions with different intensities to assess the efficacy of the RAP under different loading conditions.

1. Introduction

Following the 1964 Anchorage, Alaska, and Niigata, Japan, earthquakes, the effects and consequences of earthquake-induced soil liquefaction (liquefaction) have been intensely studied. Loose saturated granular soil that experiences liquefaction exhibits a significant decrease in shear strength due to the large increase in excess pore water pressure and a commensurate decrease in effective confining stress. Additionally, post-liquefaction consolidation can be significant and potentially damaging to infrastructure. Recent events in which liquefaction has caused damage to critical infrastructure include the 2010 Chile earthquake (M_w8.8), in which repairs to infrastructure and residential structures amounted to US$30 billion [52]; and the 2010–2011 Canterbury, New Zealand (Fig. 1), Earthquake Sequence (CES) where the damage to infrastructure amounted to NZ$40 billion [35]. Liquefaction and its mitigation remain among the most active research areas in geotechnical engineering [31]. Numerous studies have focused on understanding the physics of this phenomenon and methods to evaluate and minimize the risk due to liquefaction (e.g., Refs. [6,14,18–21]; among many others).

Construction at sites containing shallow liquefiable deposits generally necessitates either the use of deep foundations to bypass the liquefiable strata or the utilization of ground improvement (GI) methods. At an intermediate depth range (<40 ft), the former option may be less economically viable for mitigating the risk of liquefaction at large sites due to the higher cost of material and construction equipment and lengthier schedule [13,42]. Alternatively, GI techniques can be used to create a non-liquefiable crust to mitigate risk due to liquefaction [17,45,48]. Traditional GI methods such as deep dynamic compaction, vibro-compaction, compaction piles, conventional stone columns, and explosive compaction have been used with success to densify loose sands

* Corresponding author.
E-mail addresses: tat2@vt.edu (T.S. Thum), ayerro@vt.edu (A. Yerro), Asaade@gfnet.com (A. Saade), Eye@langan.com (E. Ye), KWissmann@geopier.com (K.J. Wissmann), rugreen@vt.edu (R.A. Green).

https://doi.org/10.1016/j.soildyn.2021.107088
Received 22 July 2021; Received in revised form 25 October 2021; Accepted 21 November 2021
Available online 25 November 2021
0267-7261/Published by Elsevier Ltd.

Notation

d	RAP diameter (unit: m)
d'	Equivalent RAP diameter (unit:m)
D	RAP center-to-center spacing (unit:m)
D_r	Relative density
f	Frequency (unit:Hz)
G	Shear modulus (unit:kPa)
G_0	Shear modulus coefficient
h_{p0}	Contraction rate
I_A	Arias Intensity (unit:m/s)
k	Hydraulic conductivity (unit:m/s)
K	Bulk modulus (unit:kPa)
K_0	At-rest lateral earth pressure coefficient
M_w	Moment magnitude
$N_{1,60}$	SPT N value corrected for overburden pressure and hammer efficiency
p	Mean stress (unit:kPa)
p_a	Atmospheric pressure (unit:kPa)
r_u	Excess pore water pressure ratio
$S_{a,max}$	Maximum Pseudo Spectral Acceleration (unit: g)
T_{peak}	Period corresponding to $S_{a,max}$ (unit:s)
u	Velocity-time history (unit:m/s)
V_p	Compression wave velocity (unit:m/s)
V_s	Shear wave velocity (unit:m/s)
$V_{s,across}$	Shear wave velocity measured across the RAP elements and densified soil (unit:m/s)
$V_{s,dense}$	Shear wave velocity measured in the densified soil (unit: m/s)
$V_{s,RAP}$	Shear wave velocity of the RAP elements only (unit:m/s)
γ	Unit weight (unit:kN/m^3)
γ_{xy}	Shear strain in the x-y plane
ν	Poisson's ratio
ρ	Density (unit:kg/m^3)
σ_v	Total vertical stress (unit: kPa)
τ	Shear stress (unit:kPa)

Fig. 1. Picture of post-liquefaction damage in Christchurch, New Zealand, as a result of the 2010–2011 Canterbury Earthquake Sequence. (Photo courtesy of Dr. Lukas Hogan, University of Auckland).

(e.g., Ref. [29]). However, each of these methods has associated shortcomings that prompted the development of new GI methods. These include Rapid Impact Compaction (RIC), Horizontal Soil-Cement Mixed Beams (HSM), Low Mobility Grout (LMG), Resin Injection (RES), Soil-Cement Rafts (SCR), Reinforced Gravel Rafts (RGR), and Rammed Aggregate Pier® (RAP), among others. Apart from ground densification, these GI techniques rely on mechanisms that increase liquefaction resistance by providing shear reinforcement, enhancing drainage, and increasing soil stiffness (e.g., Refs. [1,3,4,15,16,36,46]. The efficacy of these mechanisms has been observed in laboratory studies, centrifuge modeling, numerical studies, and back-analysis of field case histories (e.g., Ref. [47]). Addressing the benefits among different GI methods is beyond the scope of this paper. However, there is a need for additional field validation of the GI techniques and a better understanding of the coupled effects among the liquefaction mitigation mechanisms underlying these techniques.

Given this lack of understanding, cost-effective and reliable GI design and the implementation for critical geotechnical structures are challenging. An example of this is the Lancaster Park (formerly AMI Stadium) in Christchurch, New Zealand. The areas under the stadium stands were improved with stone columns that extended partially through a thick liquefiable layer. The site was subjected to motions during the 2011 M_w6.2 Christchurch earthquake that exceeded the design ground motions for the site, and liquefaction was triggered in the improved ground, effectively returning the improved ground to an unimproved state [2,10,54]. Unfortunately, case studies of the performance of structures founded on improved ground sites, such as the former AMI Stadium, are scarce. Also, while numerical analyses of improved ground liquefiable sites have been performed [16,38], very few use post-event field observations to validate the numerical models [49]. Moreover, none of the validated models are calibrated using full-scale test data. This is because of the substantial cost and effort associated with full-scale field testing and because only limited data can be obtained from such tests solely from physical observation and instrumentation. Thus, centrifuge data have been used as an alternative for validation of numerical models [11,12,28,37]. The numerical modeling of field tests performed on improved ground sites can complement the field data and can help verify the efficacy of GI techniques. This is especially relevant for studying liquefaction mitigation because element test and centrifuge test data may not fully replicate the in-situ hydraulic conditions and soil fabric. Furthermore, once validated, numerical models can be used to study more complex soil profiles and loading that represent a range of conditions of interest.

This study focuses on the performance of ground profiles improved with RAP subjected to ground shaking. The RAP technique densifies the ground and increases lateral stresses by driving a mandrel into the ground using combined hydraulic crowd pressure and vertical vibratory energy. Aggregate is placed in relatively thin lifts and compacted using a specially-designed tamper foot, creating dense, stiff, aggregate pier elements [53]. The objective of this paper is to investigate the mechanics of RAP elements in liquefiable soils using a calibrated and validated numerical model for dynamic conditions. The numerical modeling entails fully-coupled hydro-dynamic plane-strain FD simulations using the commercial program FLAC [22] that incorporates the PM4Sand constitutive model [5]. The numerical model is calibrated and qualitatively validated by comparing computed results with those obtained from field tests in which natural and reinforced profiles are subjected to shaking from a vibroseis (i.e., University of Texas at Austin's T-Rex) and with post-earthquake observations [39]. Finally, a parametric analysis performed with a range of ground motion intensities is performed to better understand the influence of the RAP on liquefaction mitigation.

2. Background and study overview

Following the 2010–2011 CES, a large-scale field test program was

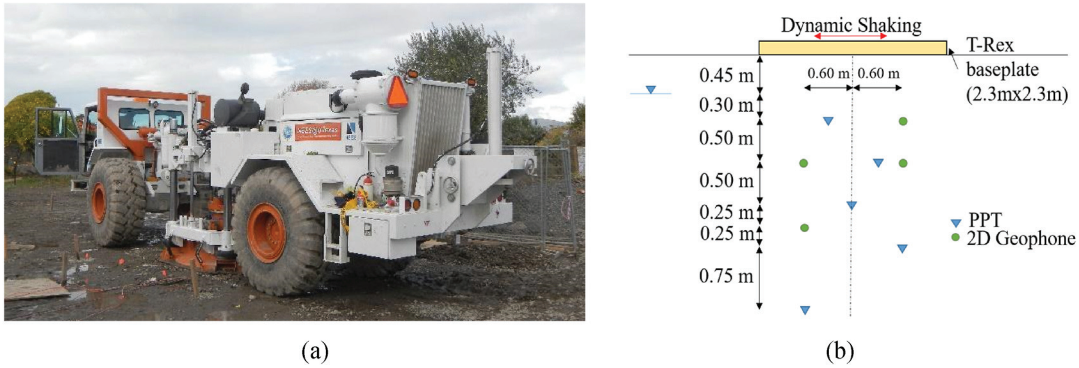

Fig. 2. Vibroseis (T-Rex) test program: (a) loading apparatus (photo courtesy of Dr. Russell Green, Virginia Tech), (b) profile showing instrumentation locations. (For interpretation of the references to colour in this figure legend, the reader is referred to the Web version of this article.)

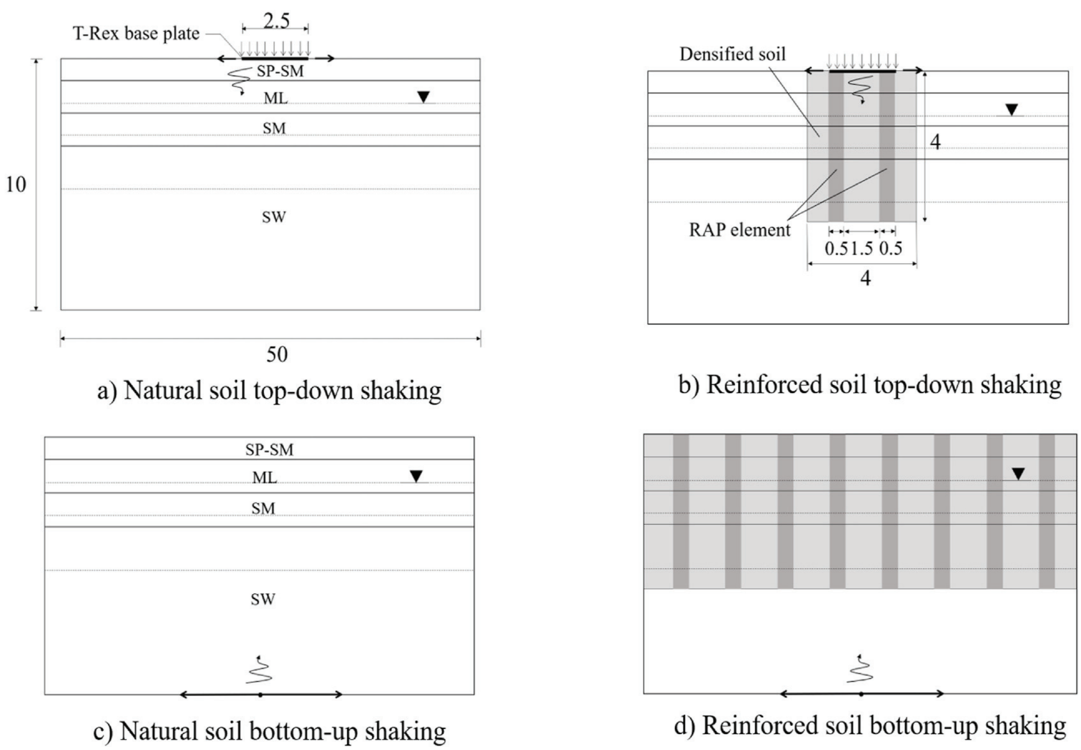

Fig. 3. Configurations of numerical models: (a) natural soil top-down shaking, (b) reinforced soil top-down shaking, (c) natural soil bottom-up shaking, and (d) reinforced soil bottom-up shaking. Darker lines indicate layer boundary, and lighter lines indicate sublayer boundary. Units in meters. Diagrams not to scale.

initiated by the New Zealand Earthquake Commission (EQC) to evaluate the efficacy of different shallow GI methods for reducing the risk due to liquefaction [39]. The Ground Improvement Programme (GIP) was conducted at three locations (Sites 3, 4, and 6) in Christchurch along the Avon River three locations [48], where severe liquefaction damage was observed during the CES. Actual locations can be found in Ref. [39]. The natural and improved subsurface conditions at the test sites were characterized with Standard Penetration Tests (SPT), Cone Penetration Tests (CPT), small-strain shear- and pressure-wave velocities (V_s and V_p) using Direct-Push Cross-Hole (DPCH) method, and trenching. As part of this GIP, eight different GI techniques were tested (e.g., Refs. [39,51,53].

Nine areas were improved using RAP at the three locations in Christchurch. Hydraulic pressure and vertical vibratory hammer energy were used to displace and densify the soil, while crushed aggregates were fed and compacted in the cavities using a beveled-shaped temper. The aggregate material used for the RAP construction comprised of open-graded gravel with minimum and maximum nominal particle sizes of 10 mm and 80 mm, respectively. The majority of aggregates used ranged between 20 and 50 mm (D_{10} to D_{90}, respectively). This resulted in 4 m long and 600 mm in diameter stiff piers. The elements were constructed in a triangular pattern spaced at a range of 1.5–3.0 m. Based on corrected CPT tip resistance performed between piers, the RAP elements effectively increased soil stiffness [51]. Small-strain shear wave velocities of densified soil between piers ($V_{s,dense}$) and across piers ($V_{s,across}$) were collected from improved subsurface using DPCH testing. The presence of the stiff piers resulted in a major increase of $V_{s,dense}$ and $V_{s,across}$ compared to shear wave velocity in natural soil profiles [51]. Among the GI methods tested, Ref. [39] concluded that the RAP elements provided the greatest increase in stiffness of the overall subsurface profiles based on CPT and DPCH testing.

The efficacy of the GI methods to mitigate liquefaction was evaluated using explosives and vibroseis (T-Rex) shaking [7,51]. The T-Rex vibroseis consists of a vehicle fitted with a square baseplate that can be loaded vertically and horizontally (Fig. 2a). The self-weight of the T-Rex

Table 1
Material properties of unreinforced (pre-RAP installation) natural soil.

Layer	Depth Range (m)	*F.C. (%)	**γ (kN/m^3)	**$N_{1,60}$	**V_s (m/s)	**G (MPa)	G_0	D_r	h_{p0}	**k (m/s)
SP-SM	0–0.5	–	17	15	102	18.2	699	0.73	0.77	9×10^{-5}
ML2	0.5–1	96	17	10	102	18.0	590	0.50	0.38	6×10^{-7}
ML1	1–1.25	74	17	5	98	16.6	457	0.33	0.93	6×10^{-7}
SM2	1.25-1.75	3–25	17	5	105	19.2	457	0.33	0.93	2×10^{-5}
SM1	1.75–2	3–25	19	10	119	27.6	590	0.44	0.57	2×10^{-5}
SW2	2–3.25	3	19	10	150	43.4	590	0.42	0.64	2×10^{-5}
SW1	3.25–10	3	19	20	155	46.7	792	0.66	0.38	7×10^{-5}

*Based on [39].
**Based on data obtained from New Zealand Geotechnical Database.

Table 2
Material properties of post-RAP installation densified soil.

Layer	Depth Range (m)	** γ (kN/m^3)	** $N_{1,60}$	**V_s (m/s)	**G (MPa)	G_0	D_r	h_{p0}	**k (m/s)
SP-SM	0–0.5	17	10	90	14.9	724	0.64	0.32	9×10^{-5}
ML2	0.5–1	16	5	94	16.2	442	0.13	1.58	6×10^{-7}
ML1	1–1.25	18	15	114	23.7	525	0.65	0.36	6×10^{-7}
SM2	1.25-1.75	18	25	140	35.9	689	0.79	1.49	2×10^{-5}
SM1	1.75–2	19	30	151	46.6	835	0.85	2.53	2×10^{-5}
SW2	2–3.25	19	35	171	59.4	954	0.88	3.31	2×10^{-5}
SW1	3.25–10	19	35	179	65.6	893	0.85	2.42	7×10^{-5}

*Based on data obtained from New Zealand Geotechnical Database.

truck imparts a vertical load equivalent to 245 kN, resulting in an average static pressure of 46 kPa beneath the baseplate. For the Christchurch testing, dynamic horizontal shaking was applied to the ground in increments with the load ranging from 1.5 to 25 kPa at a frequency of 10 Hz for 100 cycles. The sites were instrumented with geophones and pore pressure transducers (PPT) to capture the propagation of shear waves and the buildup of excess pore pressure in the subsurface, respectively (Fig. 2b) [39,51]. Specifically, 28 2D geophones having a 28 Hz resonance frequency were used to record velocity time histories, while PPTs were used to record pore pressures within the profile before, during, and after loading [39]. The data from the T-Rex testing provides a truly unique opportunity to calibrate and validate numerical models for analyzing the shaking response of natural and reinforced ground conditions.

The study presented herein entails the numerical analysis of four different scenarios comprising two subsurface conditions (i.e., natural and reinforced) subjected to two different dynamic loadings: T-Rex shaking or "top-down shaking" (Fig. 3a and b) and earthquake shaking or "bottom-up shaking" (Fig. 3c and d). The model of the natural profile is based on soil properties before the installation of the RAP, while the reinforced subsurface condition adds the RAP and a surrounding zone of densified soil. The four numerical configurations that are analyzed are illustrated in (Fig. 3). The study proceeded according to the following steps:

1. Characterization of natural and reinforced soil profiles using field data.
2. Numerical model development and calibration for the natural and reinforced profiles using T-Rex shake testing data (top-down shaking).
3. Qualitative validation of the numerical model for the natural profile using recorded earthquake ground motions and comparing predicted (bottom-up shaking) to post-event field observations.
4. Numerical parametric study of the performance of improved profiles during earthquake loading (bottom-up shaking) to provide insights into the liquefaction mitigation mechanisms of the profiles improved with RAP.

The subsequent sections of this paper are organized according to the four steps listed above in which the study progressed, expanding on the details inherent to each step.

3. Profile characterization

In-situ tests on RAP elements carried out at Site 6 (test panels 6-NS-1 and 6-NS-2) are analyzed in this study [39]. Both CPT and DPCH data are downloaded from the New Zealand Geotechnical Database [32]), whereas trench data is obtained from Ref. [39]. In particular, CPT 022 and CPT 065 are used to characterize the unimproved soil profile in test panel 6-NS-1, while CPT 060 is used to characterize the improved conditions from test panel 6-NS-2. The subsurface conditions at Site 6 generally consist of a shallow layer of poorly graded sand with silt (SP-SM) (~0.5 m thick) overlying layers of silt (ML) (~0.75 m thick), silty sand (SM) (~0.75 m thick), and clean sand (SW) (>8 m thick), as shown in Fig. 3a. Table 1 summarizes the soil layers and corresponding material parameters extending to a depth of 10 m below grade. The depth range and fines content of each layer is obtained from trench data, supplemented by CPT data for depths below the 3.3 m excavation. Unit weight (γ), relative density (D_r), SPT overburden and energy corrected blow count ($N_{1,60}$), and hydraulic conductivity (k) are correlated from CPT data using Ref. [40]. An average value for each parameter is calculated over the thickness of the layer and is assigned to the entire layer. In particular, correlations proposed by Refs. [23,26] are used to estimate D_r - both give consistent results. The hydraulic conductivity is estimated based on the normalized soil behavior index, as defined in Ref. [40].

Subsequently, V_s of the unimproved soil (natural soil) at the test panel 6-NS-2 is obtained from the DPCH soundings 35261 and 35269, which are in close proximity to the test panel. After the reinforcement, $V_{s,across}$ and $V_{s,dense}$ are obtained from DPCH 35279 at the test panel 6-RAP-1. The shear modulus (G) is obtained using Equation (1) as follows:

$$G = \frac{\gamma}{g} V_s^2 \tag{1}$$

where g is the gravitational acceleration. The remaining two parameters in Table 1 (G_0 and h_{p0}) will be discussed later in the numerical model

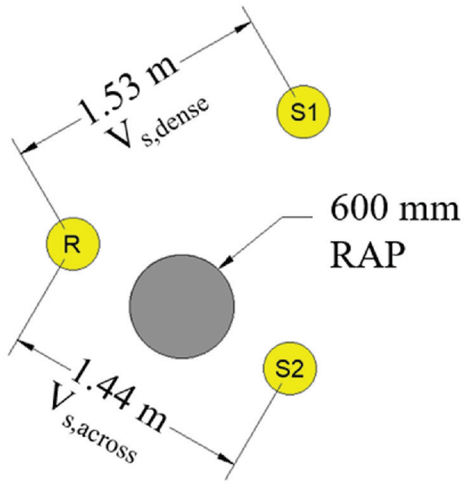

Fig. 4. Approximate location of DPCH soundings relative to RAP element. S1 and S2 represent probe sensors, while R represents the probe receiver.

Table 3
Material properties of RAP elements (based on data obtained from the New Zealand Geotechnical Database).

Depth Range (m)	P (kg/m^3)	V_s (m/s)	G (MPa)	K (MPa)	ν	K (m/s)
0–0.5	2039	555	628	1329	0.30	7×10^{-5}
0.5–1	2039	307	192	155	0.06	7×10^{-5}
1–1.25	2039	217	96	132	0.21	7×10^{-5}
1.25-1.75	2039	399	324	1708	0.41	7×10^{-5}
1.75–2	2039	574	673	3756	0.42	7×10^{-5}
2–4	2039	885	1598	3338	0.29	7×10^{-5}

section. Based on the CPT data, the depth to groundwater is estimated to be at 0.5 m beneath the ground surface [41].

Similar to natural soil parameters, the post-installation soil properties measured from the soil between the RAP elements are summarized in Table 2. A general increase in the magnitude of soil parameters with respect to the natural profile is observed, indicating a denser and stiffer condition of the site. In these conditions, liquefaction is less probable to occur because of the tendency of denser material to dilate when sheared. Note that decreases in $N_{1,60}$ and D_r are observed for the top 1 m, consistent with observations reported by Ref. [39]. This might suggest the existence of a softer and looser layer likely due to construction disturbance and subsequent lack of confinement pressure within shallow subgrade depths.

Based on the locations of the DPCH sensor and receivers relative to the installed piers (Fig. 4), $V_{s,across}$ is a composite measurement of $V_{s,RAP}$ and $V_{s,dense}$. Therefore, the shear wave velocity of the RAP elements ($V_{s,RAP}$) is de-aggregated from the composite response ($V_{s,across}$) considering the sensors' location using Equation (2), as follows:

$$V_{s,RAP} = \frac{0.6\ m}{\left(\frac{1.44\ m}{V_{s,across}} - \frac{1.44\ m - 0.6\ m}{V_{s,dense}}\right)} \tag{2}$$

where the sensor separation was 1.44 m, the diameter of the RAP was 0.6 m, and $V_{s,RAP}$, $V_{s,across}$, and $V_{s,dense}$ are in units of m/s. The shear wave velocity of the RAP elements ($V_{s,RAP}$) is then used to compute G (Equation (1)), assuming a pier density of 2039 kg/m^3. Subsequently, the bulk modulus (K) of RAP is computed using G and Poisson's Ratio values listed in Table 3. Poisson's ratio (ν) is estimated from the ratio of V_s to V_p [25] as given in Equation (3).

$$\nu = \frac{1 - 2\left(\frac{V_s}{V_p}\right)^2}{2\left[\left(1 - \frac{V_s}{V_p}\right)^2\right]} \tag{3}$$

Considering the ramming of the aggregate and associated particle degradation, and the partial infiltration of the host soil into the RAP during installation (e.g., Ref. [15]), the hydraulic conductivity of the RAP elements is assumed to be the same as the well-graded sand layer (SW2) at the site. Further discussion regarding the influence of hydraulic conductivity is presented in a later section of the paper for calibration purposes.

4. Numerical model development and calibration

4.1. General model details

The dynamic response of the natural and improved profiles is simulated using plane-strain finite difference models implemented in the commercial software FLAC 8.0 configured for large strain and dynamic formulation. To account for pore pressure changes, fully-coupled hydro-mechanical simulations are adopted to ensure simultaneous generation and dissipation of excess pore water pressure in all analyses. For simplification purposes, the geometry is defined in plane-strain conditions. The configuration of the 10 m × 50 m models is shown in Fig. 3. The use of a plane-strain model to represent the RAP elements is a significant geometric simplification. To minimize this effect, several compensating methodologies are considered in the calibration section, including the use of equivalent panel width (d') and hydraulic conductivity.

Disturbances at the RAP-soil interface and the spatial variability of the natural soil in the lateral direction are neglected. The relative displacement (slipping/gapping) is not considered between the piers and the surrounding soil. Initial stress conditions are established with elastic gravity loading and an at-rest lateral earth pressure coefficient (K_0) of 0.5. The groundwater table is set to 0.5 m below the top of the model, while the bottom boundary is impermeable. The top 0.5 m of the model are assumed to be dry during the analysis (pore pressure and degree of saturation are kept equal to zero).

Because of the absence of a distinct impedance contrast at the model base, a "quiet" (also known as "viscous" or "absorbing") boundary scheme is imposed along the bottom boundary of all the models. FLAC uses the viscous boundary formulation developed by Ref. [27]. The properties of the quiet boundaries are automatically calculated from the material immediately adjacent to the boundary; hence, the definition or calibration of additional parameters is not required [22]. Although site profile data at larger depths (>10 m) at Site 6 are very limited, a parametric analysis considering deeper profile characteristics was performed to investigate boundary effects. The results showed that the bottom boundary located at a depth of 10 m absorbs the wave reflection adequately. Different lateral boundaries are considered depending on the loading conditions. In the "top-down" shaking configurations (Fig. 3a and b), "quiet" boundaries are applied to avoid the reflection of outward waves and mimic the site conditions during the T-Rex shake testing. In addition, lateral boundaries are placed considerably far from the source load, further ensuring this condition. For the "bottom-up" shaking configurations (Fig. 3c and d), the two vertical boundaries are assumed "attached" (i.e., tied-node boundary condition). This assumption ensures identical propagation of waves on both sides of the model and minimizes unrealistic wave reflections. Note that "free-field" boundary conditions could also be used, but the flat nature of the model geometry makes the "attached" scheme more straightforward to implement. In addition, "free-field" boundary conditions are less compatible with advanced soil constitutive models (e.g., PM4Sand).

Each soil layer (in natural and densified conditions) is modeled with

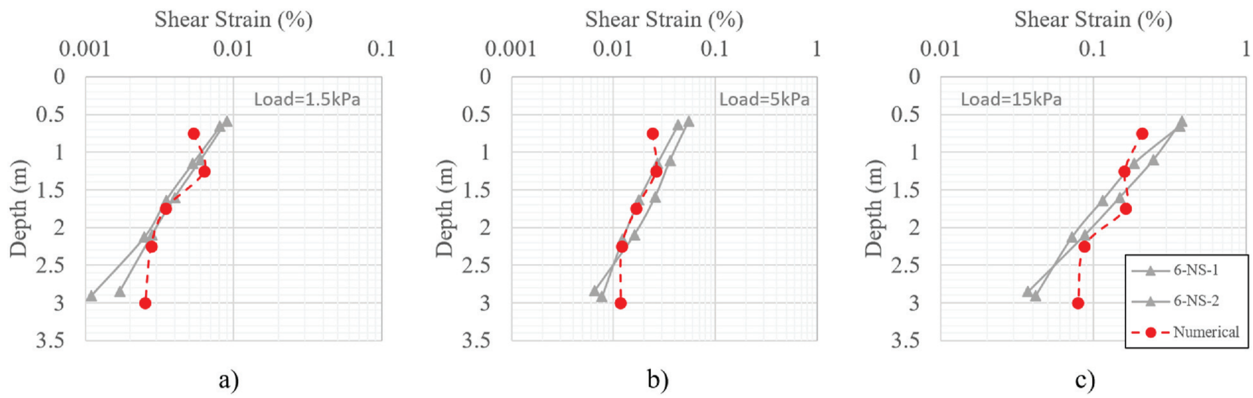

Fig. 5. γ_{xy} vs depth computed at the center of natural soil model for a top-down shaking load of: (a) 1.5 kPa, (b) 5 kPa, and (c) 15 kPa. Comparison between field data (6-NS-1 and 6-NS-2) and numerical results.

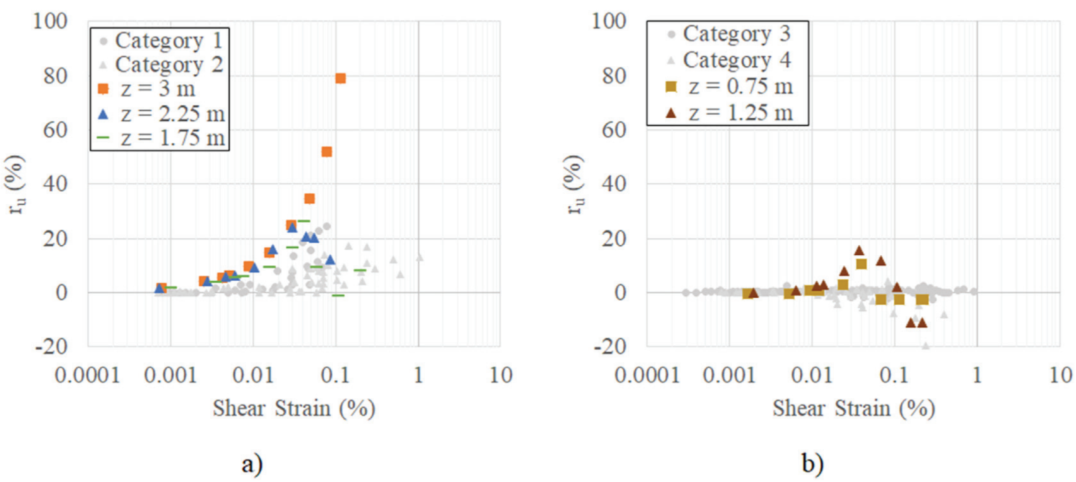

Fig. 6. r_u vs. γ_{xy} computed at the center of natural soil model for top-down shaking of: (a) liquefiable soils (Category 1 and 2), and (b) non-liquefiable soils (Category 3 and 4).

Table 4
Categories of r_u as defined in Ref. [39].

Category	Description
1	Soils that generate positive excess pore pressure and are highly susceptible to liquefaction triggering.
2	Soils that generate positive excess pore pressure but not rapidly enough to be considered highly susceptible to liquefaction triggering.
3	Soils that generate little to no none excess pore pressure regardless of shear strain level.
4	Soils that generate negative excess pore pressure.

the sand plasticity model PM4Sand (Version 3.1) because of its ability to simulate the stress-strain responses of soil for geotechnical earthquake engineering applications [5]. In particular, PM4Sand can capture the contractive/dilative response from loose/dense sand-like materials, essential to control the pore pressure generation and the liquefaction triggering. Although PM4Sand requires 21 input soil parameters, typically, only three are considered primary and are required as inputs calibrated for specific site conditions [5,30]. Recent studies have highlighted that the calibration of secondary parameters can affect the model performance [8]. However, this study uses default values for all secondary input parameters since no information from single-element laboratory testing is available. The primary inputs are the relative density (D_r), the shear modulus coefficient (G_0), and the contraction rate (h_{p0}). In particular, D_r is estimated using empirical CPT correlations as explained in the previous section. G_0 is calculated from G (determined from V_s) per Equation (4) [5]:

$$G_0 = \frac{G}{P_a\left(\frac{p}{P_a}\right)^{0.5}} \tag{4a}$$

where

$$p = \frac{1}{2}(1 + K_0)\sigma_v \tag{4b}$$

$$K_0 = \frac{\nu}{1 - \nu} \tag{4c}$$

Where P_a is atmospheric pressure in the same units as p, σ_v is the total vertical stress, and ν is Poisson's ratio. Finally, h_{p0} is used to control the contractive behavior such that a target cyclic resistance ratio is obtained [5]. This is determined from the results of single-element simulations of cyclic direct simple shear tests with stress-controlled loading, using D_r and G_0 as predicting variables. The liquefaction triggering correlation by Ref. [20] is used to get the cyclic stress ratios (CSR) needed to trigger liquefaction. This relationship provides the target CSR values for an effective overburden stress of 100 kPa and an earthquake magnitude of 7.5 in 15 uniform cycles of loading with a peak shear strain of 3% in direct simple shear loading.

The model of the improved profile includes two 4-m long RAP "panels" that are spaced 2 m on-center and a zone of densified soil surrounding the RAP panels that extends 0.75 m laterally (Fig. 3b),

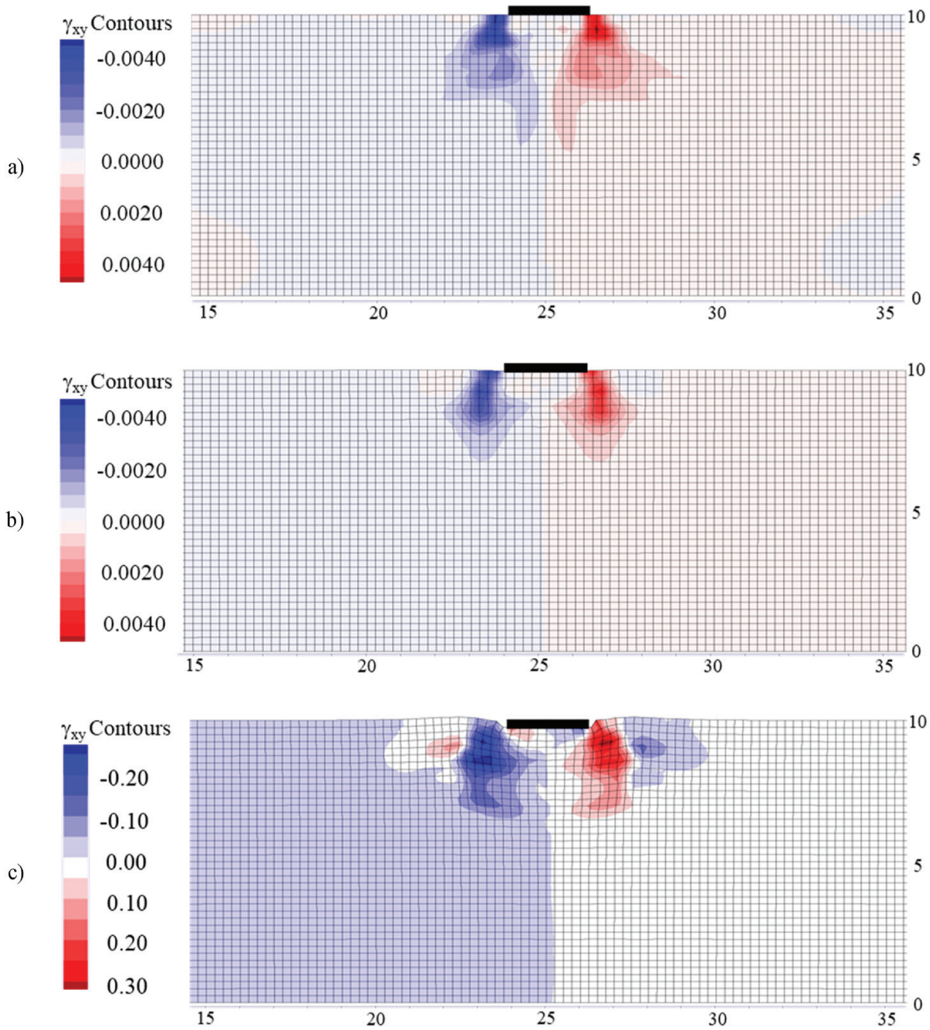

Fig. 7. Raw γ_{xy} contours of natural soil model computed at end of top-down shaking (100 cycles) load of (a) 1.5 kPa, (b) 5 kPa, and (c) 15 kPa. The baseplate is indicated on the top of the soil surface. Coordinates in meters.

consistent with the distance between sensor and receiver during DPCH testing [56]. Natural soil condition encloses the densified area. For simplification purposes and computational efficiency, RAP panels are modeled as linear elastic elements. To evaluate the impact of possible RAP non-linearities, two analyses (one for the reinforced top-down shaking model and another one for the reinforced bottom-up shaking model (Fig. 3b,d)) were performed with an elastic-perfectly plastic Mohr-Coulomb model considering a friction angle of 45° and cohesion of 0 kPa for the crushed aggregates. The results were almost identical to the results obtained with the elastic model, indicating that RAP elements essentially behave elastically for the range of stress applied within this study.

Values of the PM4Sand primary inputs for natural and densified soil profiles are summarized in Tables 1 and 2, while the RAP elastic modulus is included in Table 3.

4.2. Model calibration

The calibration of the models is performed by using GIP data collected from geophones and pore pressure transducers (PPT) for both natural and reinforced subsurface conditions during T-Rex testing post-processed by Ref. [39]. The data considered include: (a) maximum engineering shear strains (γ_{xy}) provided from filtered velocity-time records at the sensors using a displacement-based technique [9] and (b) excess pore pressure ratios (r_u) obtained from the ratio between the residual component of the excess pore pressure records and the initial effective stress.

The natural and reinforced models (Fig. 3a and b) are subjected to top-down shaking simulating the in-situ testing. The T-Rex baseplate is modeled using typical elastic structural beam elements having a total width of 2.5 m and negligible weight, located at the center top of the mesh. The beam elements are rigidly interconnected to enforce uniform vertical displacement during loading, and the rocking of the baseplate is numerically prevented. The T-Rex test is simulated by applying a static vertical load of 46 kPa onto the baseplate. Once the system achieves static equilibrium, the dynamic shear loading is applied as sinusoidal shear stress with frequency (*f*) of 10 Hz and amplitudes ranging between 1.5 and 25 kPa for a total of 100 cycles, consistent with the field test program.

Five control points along the vertical centerline of the models are used for reference; these control points are at depths consistent with the pore water pressure transducers (Fig. 2b). Computed values of shear strain in the x-y plane (γ_{xy}) consist of residual and transient components. The residual γ_{xy} corresponds to permanent displacement, while the transient γ_{xy} corresponds to the cyclic strain. In this case, transient γ_{xy} is the parameter of interest; therefore, a high-pass filter with a cut-off frequency of 2 Hz is applied to remove the residual component. Representative shear strain versus depth profiles are then generated using the maximum absolute value of the filtered data at each control point, consistent with data processing in Ref. [39]. The computed excess

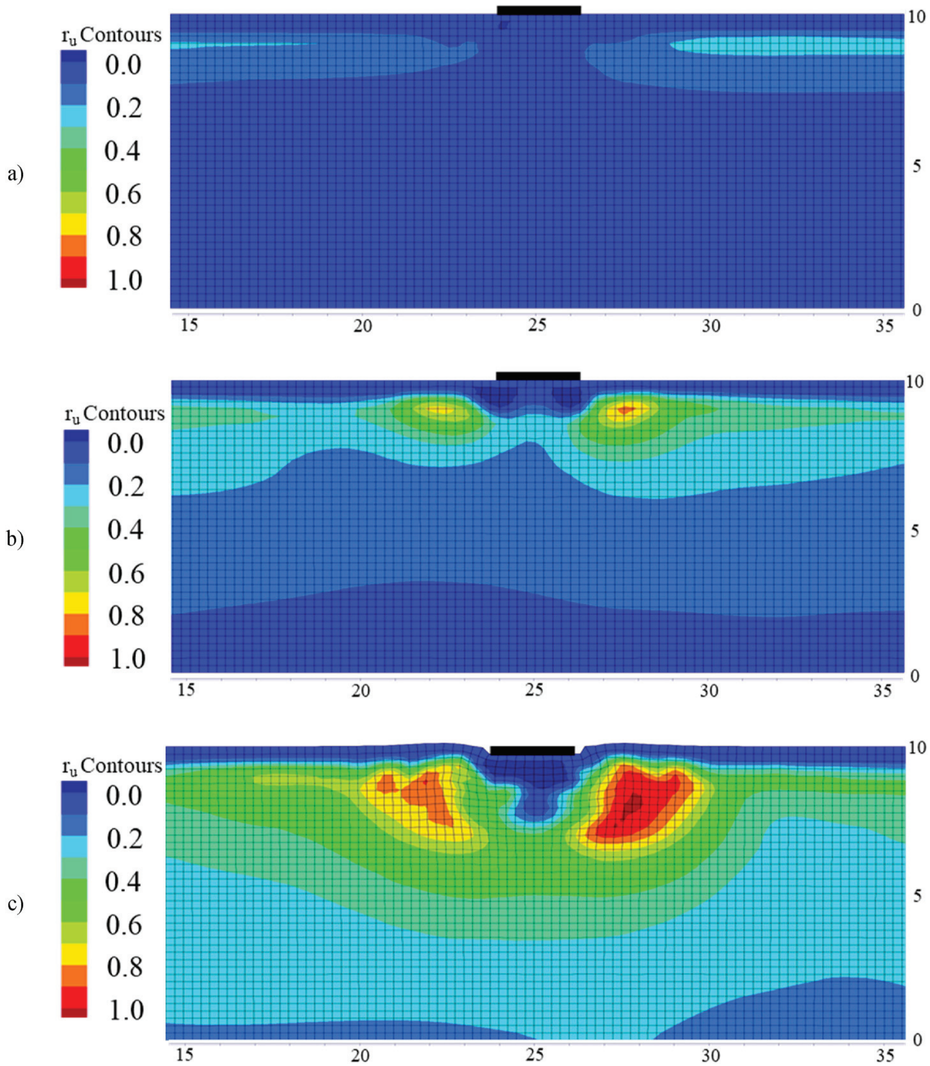

Fig. 8. Raw r_u contours of the natural soil model computed at the end of the top-down shaking (100 cycles) load of (a) 1.5 kPa, (b) 5 kPa, and (c) 15 kPa. The baseplate is indicated on the top of the soil surface. Coordinates in meters.

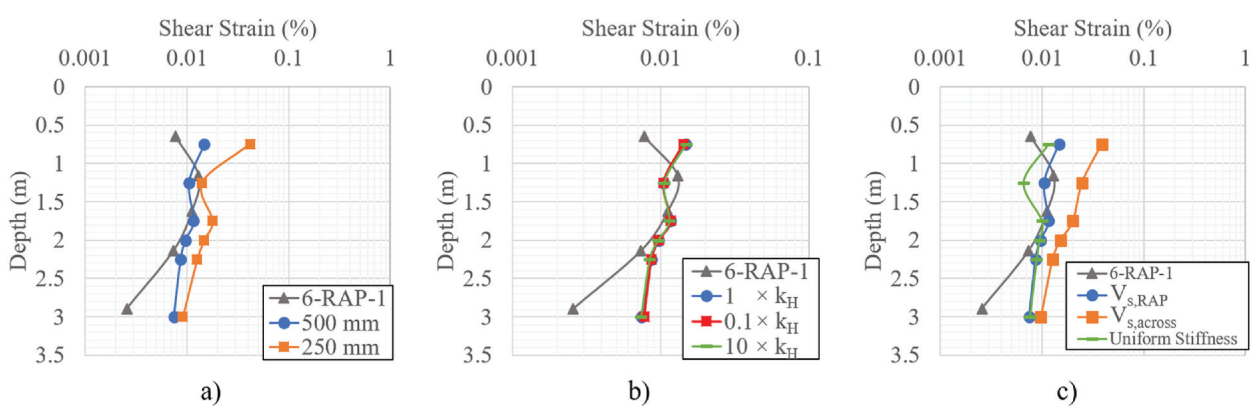

Fig. 9. γ_{xy} vs. depth profile computed at the center of the reinforced model for a top-down shaking load of 5 kPa from a parametric study of RAP: (a) width, (b) hydraulic conductivity, and (c) elastic stiffness. Comparison between field data (6-RAP-1) and numerical results.

pore water pressure ratios, r_u, are low-pass filtered with a cut-off frequency of 3 Hz to filter out transient (hydro-dynamic) responses. The cut-off frequency values are evaluated based on trial-and-error and are consistent with those in Ref. [39].

The results from the calibration analysis are presented below. While the numerical results from the natural soil profile (Fig. 3a) match the data relatively well without "tuning" the input parameters correlated from field testing, the reinforced soil model (Fig. 3b) requires a greater calibration effort.

Table 5
Material properties of RAP elements based on uniform stiffness.

Parameter	Value
Density (ρ)	2039 kg/m^3
Shear Modulus (G)	750 MPa
Poisson's Ratio (ν)	0.48
Bulk Modulus (K)	18.5 GPa

4.3. Model calibration of natural soil profile

Fig. 5 presents the measured and predicted peak shear strain profiles for the natural soil profile for three top-down shaking loads (i.e., 1.5, 5, and 15 kPa) applied by T-Rex. Each of the profiles shows a decrease in shear strain with depth and good correspondence between the measured and computed values. At a depth of 3 m, the agreement between the measured and computed values is less than for those at shallower depths. This is likely due to the inherent effects of modeling a 3D problem using a 2D plane-strain model. At shallow depths, the 2D vs. 3D effects are less significant because of the proximity of the dynamic source (i.e., 2D vs. 3D radiation damping is less significant). However, at greater distances from the dynamic source (i.e., at deeper depths), the effects of 2D vs. 3D

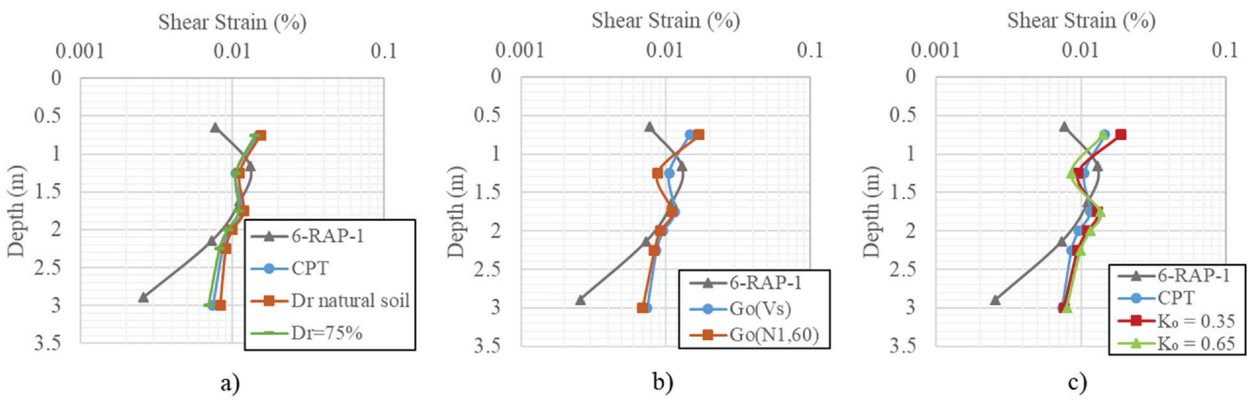

Fig. 10. γ_{xy} vs. depth profile computed at the center of the reinforced model for a top-down shaking load of 5 kPa for a parametric study of the densified soil surrounding the RAP: (a) D_r, (b) G_0, and (c) K_0. Comparison between field data (6-RAP-1) and numerical results.

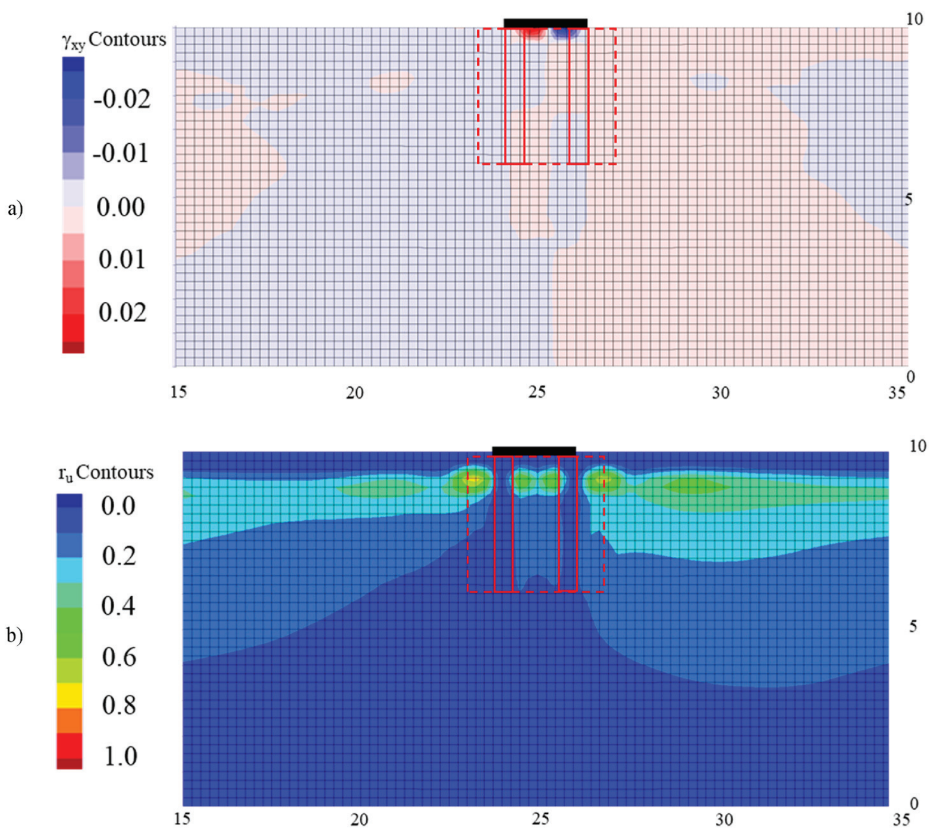

Fig. 11. Raw (i.e., pre-processed) (a) γ_{xy} and (b) r_u contours of reinforced soil model computed at the end of the top-down shaking load of 5 kPa (100 cycles). RAP and densified soil outlined in red, baseplate outlined in black. Coordinates in meters. (For interpretation of the references to colour in this figure legend, the reader is referred to the Web version of this article.)

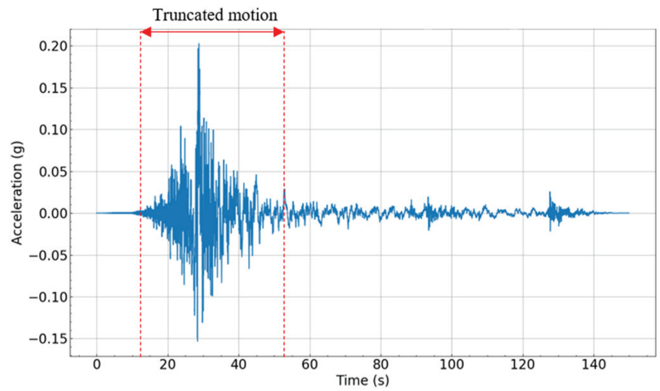

Fig. 12. Acceleration time history recorded at NNBS station during the 2010 Darfield earthquake. The truncated motion is as labeled.

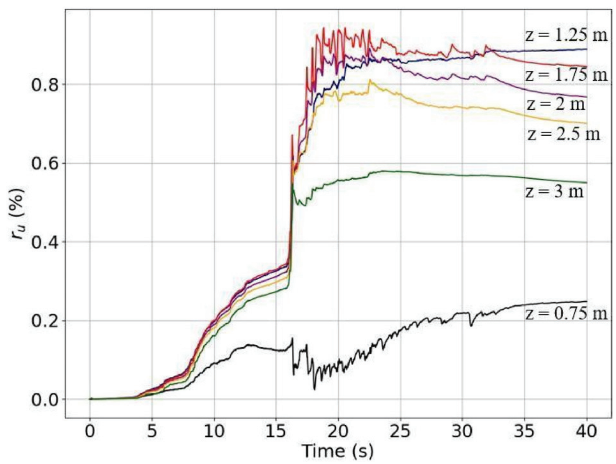

Fig. 13. r_u time history profile at the center of the natural soil model for bottom-up loading. Depths of each curve are as labeled.

radiation damping are more significant, and the energy of the shear waves may be overestimated in the 2D model, resulting in larger predicted strains.

Ref. [39] provided the measured r_u vs. shear strain at depths 0.75, 1.25, 1.75, 2.25, and 3 m for the T-Rex tests, presented as gray points in Fig. 6. Based on the trends in r_u vs. shear strain data, Ref. [39] grouped the liquefaction response characteristics of the soil into four categories (Table 4), where Categories 1 and 2 exhibit liquefaction potential, and Categories 3 and 4 do not. To further validate the numerical model, a set of dynamic simulations is performed using shear stress loading of 0.5, 1.5, 2.5, 3, 5, 7, 10, 13, 15, and 18 kPa. The computed values of r_u and shear strains at 30 cycles of loading are shown in Fig. 6, consistent with the data from Ref. [39]. Similar to the liquefaction response characteristic categories used by Ref. [39], two trends are clearly identified in the computed results: soils that exhibit liquefaction potential, consistent with Categories 1 and 2 (Fig. 6a), and soils that do not exhibit liquefaction potential, consistent with Categories 3 and 4 (Fig. 6b). The soils that exhibit liquefaction potential are those at depths of 1.75, 2.25, and 3.0 m (i.e., silty sand and well-graded sand), while the soils that do not exhibit liquefaction potential are those at depths 0.75 and 1.25 m (i.e., low plastic silt). From Fig. 6, it is observed that the numerical results match reasonably well with the field measurements presented by Ref. [39]. However, the predicted r_u values are slightly higher than the measured values, especially at a depth of 3 m. This difference may be due to higher in-situ permeability values than the ones considered in the model or due to lateral heterogeneity and soil layer variability.

Finally, to get a general idea of the overall natural soil model's response, contour plots of the raw γ_{xy} and r_u at the end of shaking for load amplitudes of 1.5, 5, and 15 kPa are presented in Figs. 7 and 8, respectively. Note that the scale in Fig. 7 changes to better represent the shear strain contours at different shaking levels. These figures show that the values of shear strain and r_u increase with applied load and clearly depict the localization of shear strain around the edges of the load plate. For a load corresponding to the 15 kPa stress, the model predicts the onset of liquefaction below the edges and surrounding perimeter of the T-Rex baseplate at depths of 1.25 m and 3 m. These predictions are in general accord with observations made during the vibroseis testing [39]. Furthermore, it is observed that the baseplate underwent an appreciable amount of settlement and soil heave surrounding it, likely due to cyclic densification.

4.4. *Model calibration of reinforced soil profile*

The calibration of the reinforced soil model is more challenging than that of the natural soil model. This is because the interfaces between the natural and densified soil surrounding the RAP, and between the densified soil and the RAP, complicate the transmission and dissipation of downward-propagating shear waves. Fig. 3b shows the cross-section of the reinforced soil model where the two RAP elements are represented as two plane-strain panels. Because the RAP elements are represented by two-dimensional panels, the equivalent panel width (d') needs to be determined to minimize the 2D vs. 3D effects and its influence on correlated material parameters. Towards this end, the calibration process mainly relies on determining the equivalent width and the hydraulic conductivity of the RAP panels. In addition, to determine the impact of other key input parameters on the system's dynamic response, a sensitivity analysis is performed on the RAP panels' stiffness and the relative density, and the stiffness, and at-rest lateral earth pressure coefficient of the densified soil. The final selection of these parameters is based on the comparison of the computed response with field measurements.

Ref. [33] proposed several methodologies for modeling a 3D array of reinforcing elements as 2D panels in plane-strain analyses. These methodologies result in reducing the width of the modeled 2D panels to obtain equivalency in (a) area, (b) moment of inertia, or (c) section modulus to the 3D array of reinforcing elements. Considering the actual diameter ($d = 0.6$ m) and center-to-center spacing (D) of the RAP elements installed at Site 6, the three methodologies are applied to obtain the equivalent RAP diameters, d' (or RAP panel widths). Using $V_{s,RAP}$, the calculated d' ranges from 0.12 m to 0.44 m. Based on these results and maximizing the mesh regularization of the model, two numerical models are constructed considering equivalent RAP diameters of 0.25 m and 0.5 m. The shear strain profiles for the two models are evaluated and compared to field measurements, as shown in Fig. 9a. It may be observed that the magnitude of the shear strain increases slightly when the equivalent RAP diameter decreases, but the difference is small. An equivalent RAP diameter of 0.5 m is chosen as the default value for further analyses due to its better agreement with field data.

The 2D vs. 3D effects also influence the dissipation of excess pore water pressures, as does the selected equivalent diameter of the RAP. To assess the influence of these on the model response, three models are analyzed considering RAP elements with hydraulic conductivities (k) of 0.1, 1, and 10 times the values reported in Table 3. Fig. 9b shows that a 10-fold increase or decrease of RAP hydraulic conductivity values has little influence on the computed shear strains, suggesting that RAP hydraulic conductivity is not an important mechanism for reducing shear strains in this loading configuration.

As mentioned above, the RAP stiffness used in the previous analyses is based on $V_{s,RAP}$, which is extracted from the $V_{s,across}$ measurements using Equation (2). To assess the validity of this approach, an additional simulation is carried out with the elastic properties of RAP elements based on $V_{s,across}$ directly. Also, considering that RAP elements are often designed assuming constant properties along their length, an additional

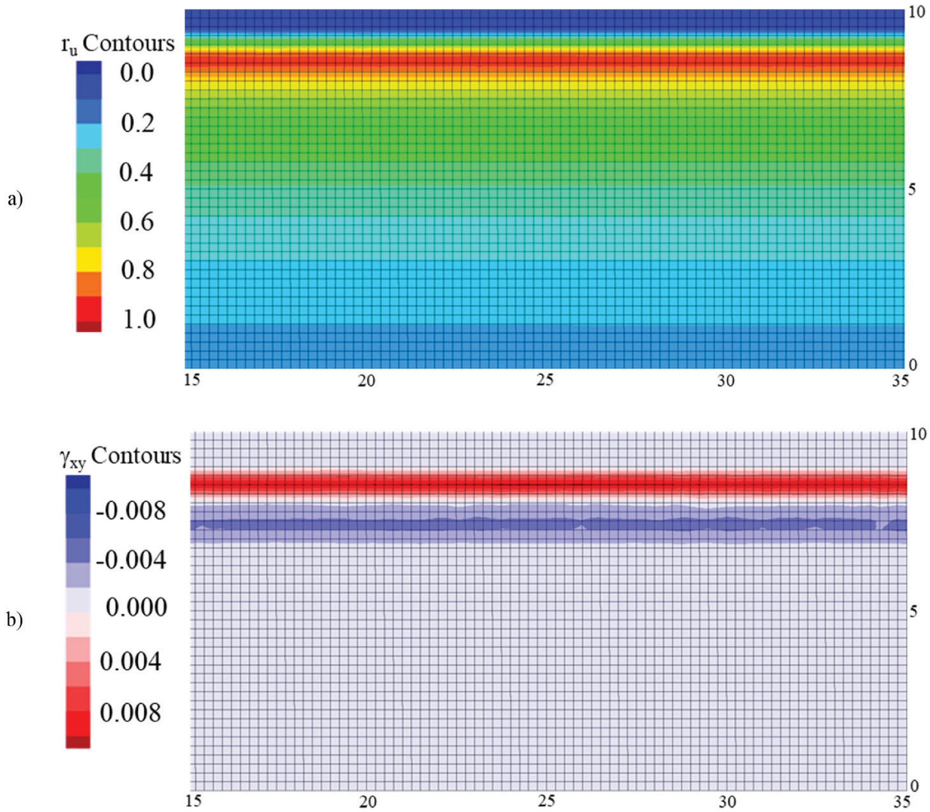

Fig. 14. Raw (a) r_u and (b) γ_{xy} contours of the natural soil model computed at the end of the bottom-up shaking (40 s). Coordinates in meters.

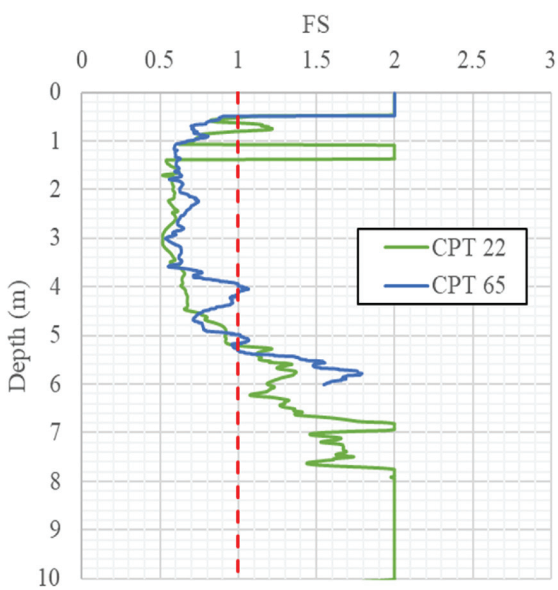

Fig. 15. Factor of safety (FS) against liquefaction at Site 6 (CPT 022 and CPT 065) during 2010 Darfield earthquake. Based on [44].

analysis is performed assuming constant stiffness RAP elements (Table 5). The results are presented in Fig. 9c. The assumption of a constant stiffness along the length of the RAP element results in shear strains that are less in the silty layers but matches the $V_{s,RAP}$-based model in the deeper sandy layer. These trends highlight that the stiffness of the RAP might be less in strata that are loose/soft and provide less lateral constraint. Furthermore, the $V_{s,across}$-based model results in an over-prediction of the shear strains for the entire depth of the reinforced

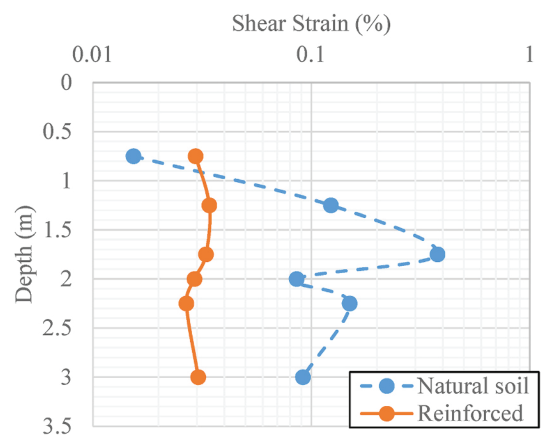

Fig. 16. γ_{xy} vs. depth profile computed at the center of natural soil and reinforced model for bottom-up shaking.

zone, highlighting the shortcomings of using a composite stiffness for the reinforced zone. In combination, these results highlight the importance of the stiffness of the RAP elements on the induced shear strains.

Similar to the parametric study performed to assess the influence of various RAP parameters on the model response, a sensitivity study is also performed to evaluate the parameters for the densified zone surrounding the RAP. Specifically, the influence of D_r, G_0, and K_0 of the densified zone on the model response is considered. In the previous simulations, the D_r of the densified soil is estimated through correlations with CPT measurements [23,26]. This is different from the correlation suggested by Ref. [5]. Fig. 10a shows the influence of increasing the relative density of the densified zone from the soil's pre-RAP-installation D_r (Table 1) to D_r = 75% [43], with a corresponding change in the contraction rate parameter value (h_{p0}). These results show that the D_r of

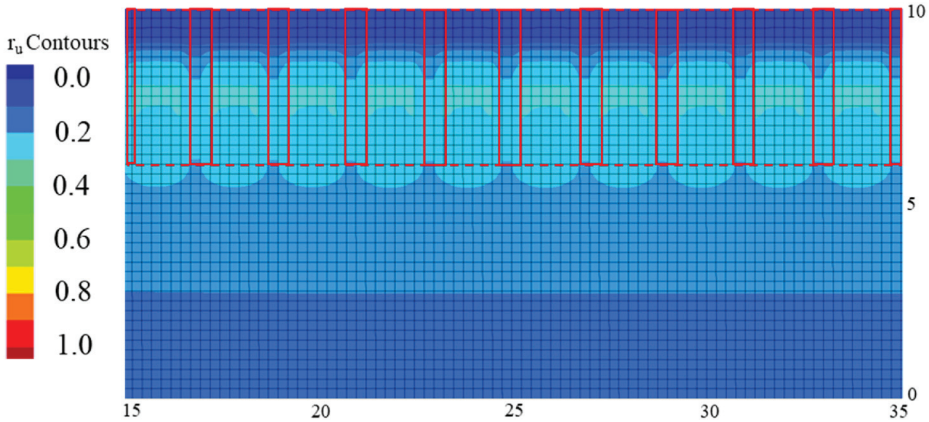

Fig. 17. Contours of raw *ru* for reinforced soil model computed at the end of bottom-up shaking. RAP and densified soil outlined in red. Coordinates in meters. (For interpretation of the references to colour in this figure legend, the reader is referred to the Web version of this article.)

Table 6
Additional ground motions (based on PEER NGA-West2 Database [34]).

Event Name	Year	Station	Magnitude	PGA (g)	$S_{a,max}$ (g)	T_{peak} (s)	I_A (m/s)
Darfield, New Zealand	2010	North New Brighton School	7.0	0.1	0.54	0.25	0.17
Christchurch, Canterbury	2011	North New Brighton School	6.2	0.35	1.15	0.08	0.24
White Narrows	1987	Garvey Reservoir	5.99	0.38	0.52	0.18	0.96
Chalfant Valley	1986	Tinemaha Reservoir	6.19	0.04	0.17	0.40	0.02
Palm Springs	1986	Tule Canyon	6.06	0.11	0.38	0.29	0.06
Morgan Hill	1984	Coyote Lake Dam SW Abutment	6.19	0.71	2.89	0.26	2.88
Kocaeli	1999	Gebze	7.51	0.24	0.67	0.40	0.55
Chi-chi	1999	ILA031	6.2	0.08	0.18	0.28	0.10
Kobe	1995	KJM	6.9	0.82	3.33	0.34	8.39
San Fernando	1971	Maricopa Array #2	6.61	0.01	0.04	0.30	0.00
Northridge	1994	West Covina - S Orange Ave	6.69	0.06	0.25	0.20	0.08
Landers	1992	Calabasas - N Last Virg	7.28	0.01	0.05	0.30	0.01

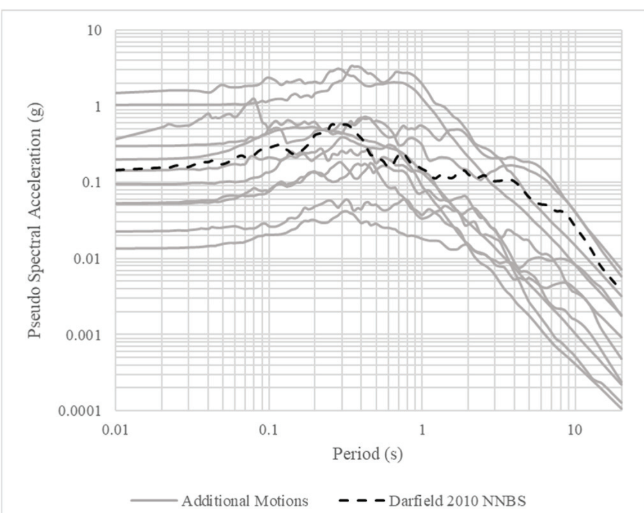

Fig. 18. Pseudospectral response spectra at damping ratio of 5% of the ground motions used in this study. The scaled Darfield 2010 NNBS motion is shown as a dashed line.

the densified zone has little influence on the computed shear strains. Fig. 10b and c further show that the computed results are not very sensitive to selected values for G_0 (based on either V_s and $N_{1,60}$) or K_0.

Contour plots of raw (i.e., before processing) γ_{xy} and r_u computed at the end of the shaking (5 kPa) for the calibrated reinforced soil model are presented in Fig. 11. Fig. 11a clearly shows that the shear strains concentrate between the RAPs, just beneath the baseplate. As expected, the presence of the relatively stiff RAP elements and densified zone surrounding the RAP elements resulted in reduced shear strains as compared to the natural soil model. Fig. 11b shows r_u contours and, to some extent, the reduction of excess pore pressure buildup between the RAP elements and densified soil.

4.5. Summary

The calibrated models show good correspondence between the measured and computed shear strains and r_u values over most of the reinforcement depth. The overestimated shear strains at a depth of 3 m likely result from the radiation of shear waves in three dimensions during T-Rex testing (especially at deeper depths) compared to the numerical model, in which shear waves only travel within a 2D plane. The results also indicate that the stiffness properties (shear modulus and bulk modulus) of the RAP columns control the response of the reinforced model when subjected to top-down cyclic loading. In contrast, the RAP hydraulic conductivity, panel width, the increase in relative density in surrounding soil, and the increase of lateral earth pressure have less influence on the computed shear strains.

5. Qualitative validation of the numerical model with field observations

The calibrated model for the natural profile is assessed by applying earthquake motions from the CES (i.e., bottom-up shaking) and comparing the predicted liquefaction response of the profile to post-event field observations. The analysis is performed using the ground

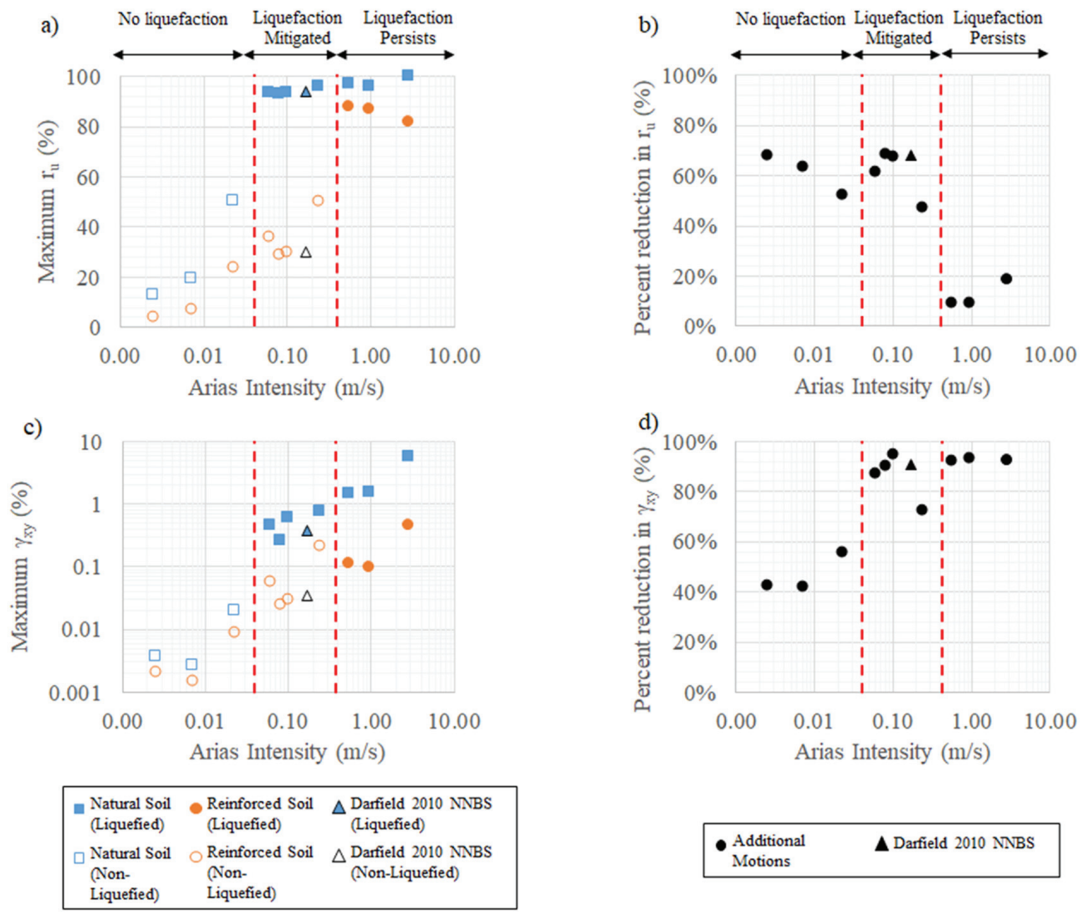

Fig. 19. Plots of (a) maximum r_u, (b) percent reduction in r_u, (c) maximum γ_{xy}, and (d) percent reduction in γ_{xy} as a function of I_A measured at the centerline between two RAP panels. For plots (a) and (c), the filled symbols indicate liquefaction is triggered, whereas empty symbols indicate liquefaction did not triggered.

motions recorded at the North New Brighton School (NNBS) station during the M_w7.1 Darfield earthquake (September 4, 2010), the largest event in the CES (Fig. 12). The NNBS station is the closest recording station to Site 6, where the RAP testing was performed [55]. The NNBS ground motion is deconvolved to the depth corresponding to the base of the FLAC model using the 1D site response analysis program STRATA [24]. To account for the influence of multi-directional shaking on liquefaction triggering in a 2D plane-strain model, the deconvolved NNBS motion is scaled by a factor of 1.11 and used as an input at the base of the FLAC model. This scaling factor is based on Ref. [44]; which recommends reducing the liquefaction resistance determined in a 1D cyclic simple shear test by a factor of 0.9 to account for multi-directional shaking. Therefore, the inverse (i.e., $1/0.9 = 1.11$) needs to be accounted for in the proposed model. The motion is converted to shear stress (τ) time history using Equation (5) and truncated to a total duration of 40 s to reduce unnecessary computational time.

$$\tau = 2\rho V_s u \tag{5}$$

where ρ and V_s are the density and small-strain shear wave velocity of the soil at the base of the FLAC model, respectively, and u is the velocity-time history at the base of the FLAC model (i.e., "quiet" boundary).

Fig. 13 presents the r_u vs. time plot computed along the vertical centerline of the model at six different depths. The simulation shows that, as expected, r_u increases with time during the shaking until it reaches a stable value at ~25 s. The maximum r_u computed at depths 1.25 and 1.75 m is the highest (>0.8), followed by r_u at depths of 2 m (0.75), 2.5 m (0.7), and 3 m (0.55). The lowest r_u is at 0.75 m (0.2), which can be attributed to its proximity to the depth of the groundwater table, resulting in rapid dissipation of the excess of pore water pressures.

For all intents and purposes, $r_u \geq 0.8$ indicates that liquefaction is predicted to have triggered in the field. As shown in Table 1, the subsurface soil grades from silt (depth of 0.75 m) to silty sand (depths of 1.25 and 1.75 m) to well-graded sand (depths of 2–3 m) with depth. The computed r_u values are consistent with the liquefaction susceptibility of the soil layers in the model. Fig. 14a shows the pattern of computed r_u values at the end of the shaking. It is observed that $r_u > 0.8$ for the entire silty sand and well-graded sand layers located between 1 and 2 m deep. Fig. 14b shows calculated shear strains with the highest values corresponding to layers with high r_u values.

The results of the bottom-up analysis for the natural soil profile are consistent with field observations [50] that indicate that Site 6 liquefied due to the shaking during the Darfield event. These results are also consistent with the liquefaction analysis performed by Ref. [44] for Site 6 utilizing the CPT-based simplified liquefaction triggering procedure proposed by Ref. [18]. The liquefaction-triggering analysis indicates that soil layers with higher liquefaction potential are concentrated within the top 4 m below the groundwater table (Fig. 15).

There are no sites in Christchurch that were improved with RAP and subjected to the CES events, and hence, a similar validation exercise cannot be performed for the calibrated model for the RAP reinforced profile. However, given the parallel paths followed to calibrate the natural and reinforced profiles, and the validity of the calibrated natural profile model, by supposition, it is assumed that the calibrated model of the reinforced profile is also "valid." Accordingly, to assess the efficacy of the RAP on mitigating liquefaction, the reinforcement is extended across the model's width to simulate a realistic scenario used in ground improvement projects (Fig. 3d) and subjected to the same motion used to validate the natural profile model. Fig. 16 compares the computed

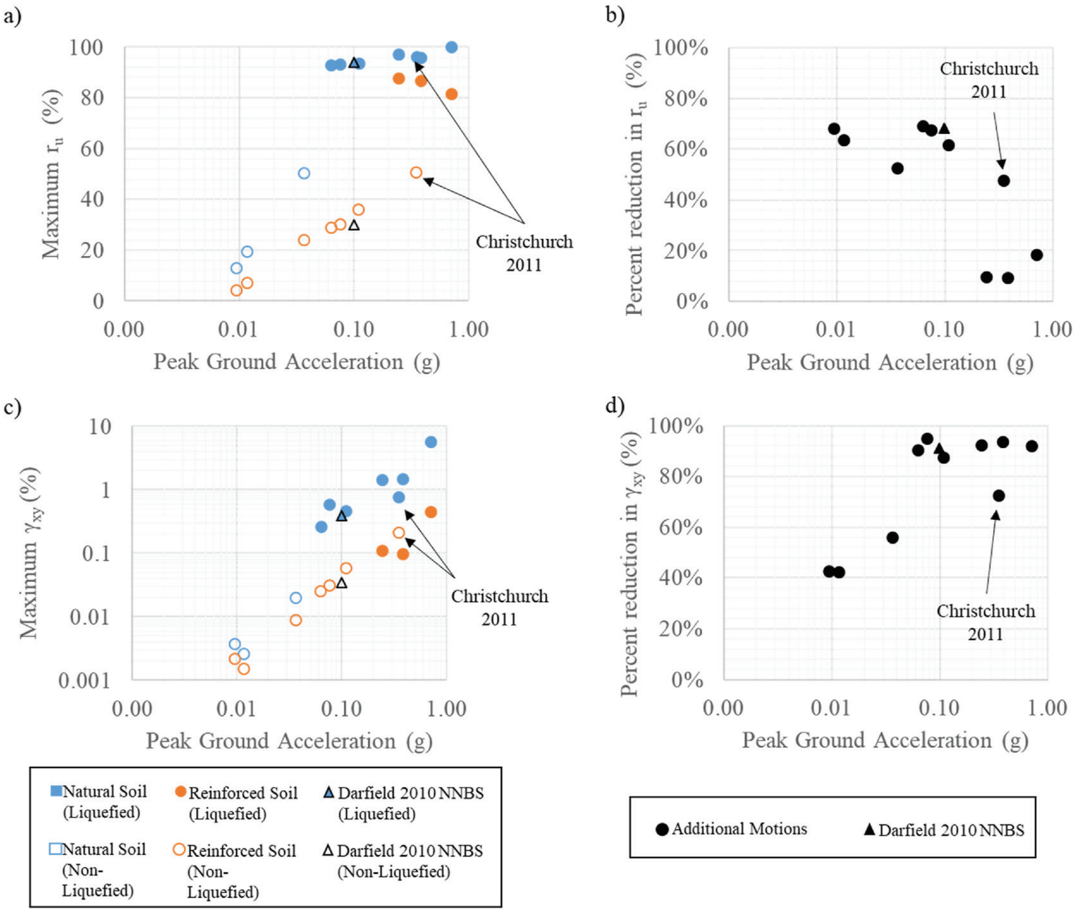

Fig. 20. Plots of (a) maximum r_u, (b) percent reduction in r_u, (c) maximum γ_{xy}, and (d) percent reduction in γ_{xy} as a function of PGA measured at the centerline between two RAP panels. For plots (a) and (c), the filled symbols indicate liquefaction is triggered, whereas empty symbols indicate liquefaction did not triggered.

shear strains at the vertical centerline of the model for both unreinforced and reinforced conditions. The shear strains computed for the reinforced soil profile are generally more uniform with depth and about 30% smaller than those for the natural (or unreinforced) profile. Fig. 17 shows that the computed maximum r_u values for the reinforced soil profile are approximately 0.3. These values are much lower than those calculated for the same unreinforced layers at depths of 1.25 m and 1.75 m, where r_u is computed to be approximately 0.8. The comparison of Figs. 16 and 17 clearly shows that the presence of the relatively high stiffness RAP elements significantly reduces shear strains and the resulting excess pore water pressures.

6. Parametric study

To better understand the influence of the RAP on liquefaction mitigation for a range of ground motion intensities, the qualitatively validated natural (or unreinforced) and reinforced models (Fig. 3c and d) are subjected to eleven different input motions (Table 6), each from a different magnitude event and ranging in frequency content and duration. The pseudospectral response spectra of the motions are presented in Fig. 18. The maximum pseudo spectral acceleration value ($S_{a,max}$) at damping ratio of 5% of each motion and its corresponding period are included in Table 6. The ground motions were obtained from the PEER NGA-West2 Database [34], truncated based on the first and last exceedance of 0.005g acceleration to minimize the computational time.

The computed maximum r_u and γ_{xy} during shaking are correlated to different input ground motion parameters, including Arias Intensity (I_A), peak ground acceleration (PGA), and $S_{a,max}$, without site effects considered. The best correlation is achieved with I_A, consistent with the notion that this parameter value reasonably quantifies the characteristics of the ground motion by a single value. Fig. 19 shows correlations between I_A and computed maximum shear strain and excess pore water pressure, with both r_u and γ_{xy} increase with I_A of the input motion. As before, assuming $r_u \geq 0.8$ indicates liquefaction is triggered, the results shown in Fig. 19 highlight three different scenarios: (a) when $I_A < 0.04$ m/s, liquefaction is not predicted to occur for either the natural or reinforced conditions; (b) when 0.04 m/s $< I_A < 0.4$ m/s, liquefaction is predicted to occur for the unreinforced conditions but not for the reinforced conditions; and (c) when $I_A > 0.4$ m/s, liquefaction is predicted to occur for both the natural and reinforced conditions. In all cases, the inclusion of RAP leads to a reduction of r_u (Fig. 19b). For the conditions described herein, the r_u reduces an average of 61, 63, and 12% for each range of I_A (i.e., $I_A < 0.04$, 0.04 m/s $< I_A < 0.4$, and $I_A > 0.4$).

Using the same I_A grouping for the shear strain plots, the results of the analyses show that liquefaction is mitigated when the maximum induced γ_{xy} is less than 0.08% (Fig. 19c). The inclusion of the RAP reduced the induced shear strains by 40–60% when $I_A < 0.04$ m/s and 70–95% when $I_A \geq 0.04$ m/s (Fig. 19d). Note that because I_A is a function of the frequency content of the input ground motions, it is not likely that the identified thresholds for I_A corresponding to the different liquefaction responses of the profiles universally apply to all profiles. Rather, it is likely that similar trends will hold, but thresholds for I_A corresponding to the different liquefaction responses will be dependent on the response characteristics of a given profile.

For completeness, Figs. 20 and 21 show the correlations to PGA and $S_{a,max}$ at damping ratio of 5%. Both intensity measures also differentiate the three scenarios described by I_A. For PGA < 0.06 g and $S_{a,max} < 0.18$ g, liquefaction is not predicted for both natural and reinforced soil

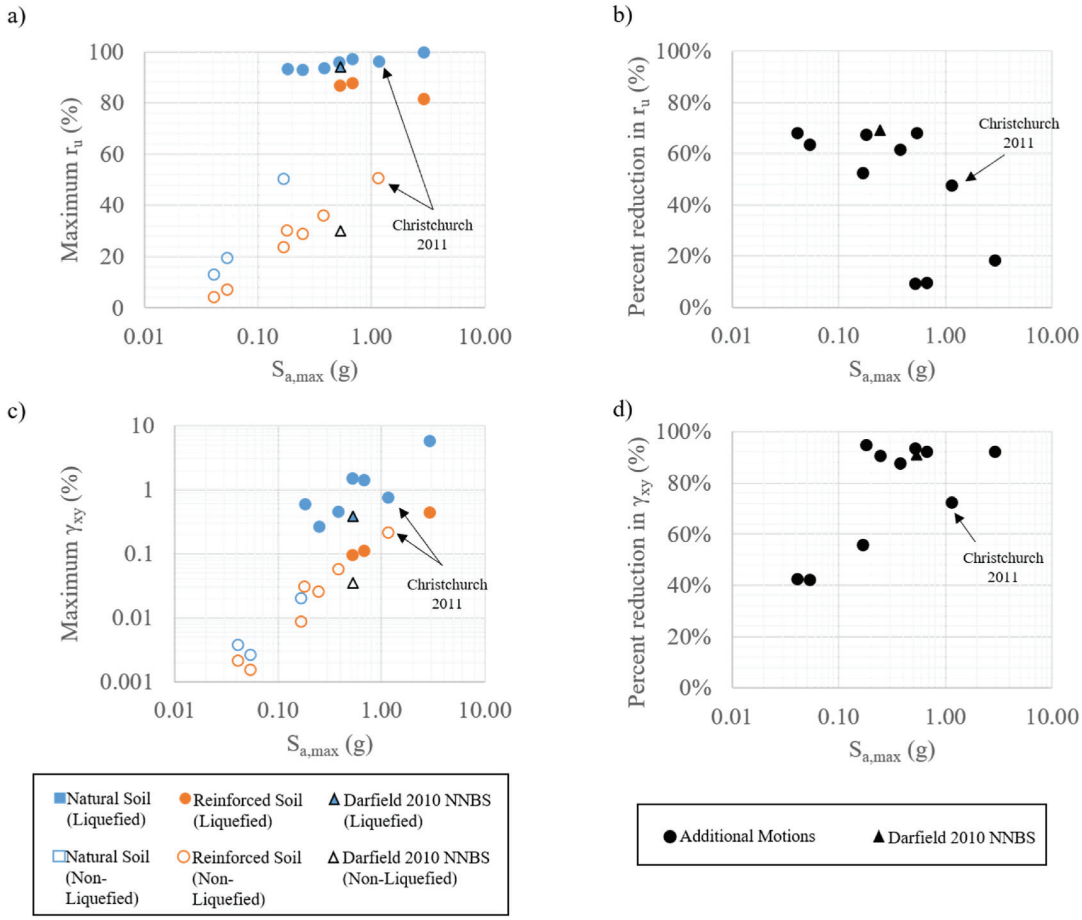

Fig. 21. Plots of (a) maximum r_u, (b) percent reduction in r_u, (c) maximum γ_{xy}, and (d) percent reduction in γ_{xy} as a function of $S_{a,max}$ at damping ratio of 5% computed at the centerline between two RAP panels. For plots (a) and (c), the filled symbols indicate liquefaction is triggered, whereas empty symbols indicate liquefaction did not triggered.

conditions (scenario a), whereas liquefaction is mitigated for 0.06 g $\leq$ PGA$<$ 0.24 g and 0.18 g $\leq S_{a,max} <$ 0.52 g (scenario b). However, for PGA$\geq$ 0.24 g and $S_{a,max} \geq$ 0.52 g, the grouping is less obvious due to an outlier case corresponding to the motion recorded at NNBS station during the Christchurch 2011 event. In the case of $S_{a,max}$, the Darfield 2010 event also borders the mitigated and non-mitigated zone. Therefore, the I_A is believed to be the best indicator for the range of liquefaction mitigation efficacy.

7. Conclusions

This paper presents, to the best of the authors' knowledge, the first study performed on a specific ground improvement methodology that uses detailed site characterization, large-scale field test data, and post-earthquake field performance observations to calibrate and qualitatively validate a numerical model. The numerical analyses consisted of 2D fully-coupled hydro-mechanical finite-difference plane-strain simulations in natural and reinforced subsurface conditions. The calibration exercise consisted of comparing the numerical results with vibroseis test (T-Rex) data while varying a few input parameters (e.g., RAP panels' width and hydraulic conductivity). The calibrated natural soil profile model is then qualitatively validated by applying scaled earthquake ground motions from the 2010–2011 Canterbury, New Zealand, Earthquake Sequence to the bottom of the model and comparing computed results with field observations. Parallel paths were followed to calibrate the natural and reinforced profiles. This, given the validity of the calibrated natural profile model to both top-down and bottom-up shaking, by supposition, it is assumed that the calibrated reinforced profile, which was validated for top-down shaking, is also valid for bottom-up shaking. Accordingly, the reinforced soil model is then subjected to eleven different scaled ground motions representing a range of earthquake magnitudes, frequency contents, and durations.

The conclusions of this study are as follows, which summarize the performance of RAP for conditions similar to those described in this paper:

1. Calibrated numerical models can be effective for providing insights into the complex mechanisms associated with liquefaction mitigation in treated ground.
2. RAP reinforcement reduces the shear strains in the reinforced layer to approximately 10%–30% of those values in unreinforced ground. This reduction in shear strain results in a reduction in excess pore water pressure, with the maximum r_u in the most-susceptible layer decreasing from 80% to 30%.
3. The efficacy of the RAP reinforcement is dominated by the stiffness of the RAP elements in comparison to the natural soil. A good match between the computed and measured results is achieved when the "ture" shear wave velocity of the RAP panels is back-calculated from the measured value of the RAP and surrounding densified soil. The panel width is determined such that its moment of inertia is consistent with that for the columnar elements.
4. The density, K_0, initial stiffness, and hydraulic conductivity of the soil immediately surrounding the RAP elements had a relatively small effect on the calibration procedure and computed results.
5. A correlation is observed between the liquefaction response of the profiles and the I_A of the input motion. However, it is noted that

because I_A is a function of the frequency content of the input ground motions, it is not likely that the identified thresholds for I_A corresponding to the different liquefaction responses of the profiles universally apply to all profiles. Rather, it is likely that similar trends will hold, but thresholds for I_A corresponding to the different liquefaction responses will be dependent on the response characteristics of a given profile.
6. These results should be used to inform further analysis performed in full 3D conditions to better understand the performance of RAP and fully evaluate the 3D effects and multi-directional response of the system.

Data availability statement

Some or all data, models, or code that support the findings of this study are available from the corresponding author upon reasonable request.

Credit author statement

Tat S. Thum: Formal analysis, Writing - Original Draft; **Alba Yerro**: Conceptualization, Methodology, Formal analysis, Writing - Review & Editing, Supervision; **Angela Saade**: Formal analysis; **Evin Ye**: Formal analysis; **Kord J. Wissmann**: Conceptualization, Writing - Review & Editing, Funding acquisition; **Russell A. Green**: Writing - Review & Editing.

Declaration of competing interest

The authors declare that they have no known competing financial interests or personal relationships that could have appeared to influence the work reported in this paper.

Acknowledgements

This research is partially funded by Geopier Foundation Company and National Science Foundation (NSF) Grant Numbers CMMI-1825189 and CMMI-1937984. This support is gratefully acknowledged. The authors extend thanks to Drs. Ken Stokoe and Brady Cox, the University of Texas at Austin, for discussions on the T-Rex field testing, and to Dr. Jorge Macedo, Georgia Tech, for his constructive recommendations on the numerical modeling. However, any opinions, findings, and conclusions, or recommendations expressed in this paper are those of the authors. They do not necessarily reflect the views of Geopier Foundation Company, NSF, or others.

References

[1] Adalier K, Elgamal A, Meneses J, Baez JI. Stone columns as liquefaction countermeasure in non-plastic silty soils. Soil. Dynam. Earthq. Eng 2003;23(7):571–84.
[2] Alexander GJ, Arefi J, Wotherspoon LM, Stolte AC, Cox BR, Green RA, Wood CM. A case study of stone column ground improvement performance during a sequence of seismic events. Rome, Italy. Proc. 7th international conference on earthquake geotechnical engineering (7ICEGE). 2019. 17-20 June 2019.
[3] Ashford SA, Rollins KM, Bradford SC, Weaver TJ, Baez JI. Liquefaction mitigation using stone columns around deep foundations: full scale test results. Transport Res Rec 2000;1736:110–8.
[4] Baez JI. A design model for the reduction of soil liquefaction by using vibro-stone columns. Ph.D. thesis. Los Angeles, CA: Univ. of Southern California; 1995.
[5] Boulanger RW, Ziotopoulou K. PM4Sand (Version 3.1): a sand plasticity model for earthquake engineering applications. Davis, CA: Center for Geotechnical Modeling, (UCD/CGM-15/01), University of California at Davis; 2017. p. 112.
[6] Boulanger RW, Idriss IM. CPT and SPT based liquefaction triggering procedures. Davis, CA: Center for Geotechnical Modeling, (UCD/CGM-14/01), University of California at Davis; 2014. p. 134.
[7] Chang W-J, Rathje EM, Stokoe II KH, Cox BR. Evaluation of effectiveness of prefabricated drains in liquefiable sand. Soil Dynam Earthq Eng 2004;24(9– 10): 623–731.
[8] Chen L. Implementation, verification, validation, and application of two constitutive models for earthquake engineering applications. Ph.D. thesis. Seattle, WA: University of Washington; 2020.
[9] Cox BR. Development of a direct test method for dynamically assessing the liquefaction resistance of soils in situ. Ph.D. thesis. Austin, TX: University of Texas at Austin; 2006.
[10] Cubrinovski M, Green RA, Wotherspoon LM, editors. "Geotechnical Reconnaissance of the 2011 Christchurch, New Zealand earthquake." Geotechnical Extreme Events Reconnaissance Association (GEER); 2011. http://geerassociation.org/.
[11] Demir S, Özener P. Numerical investigation of seismic performance of high modulus columns under earthquake loading. Earthq Eng Eng Vib 2019;18(4): 811–22.
[12] Esmaeili M, Hakimpour SM. Three dimensional numerical modelling of stone column to mitigate liquefaction potential of sands. J. Seismol. Earthquake. Eng. 2015;17(2):127–40.
[13] Farrell T, Taylor A. Rammed aggregate pier design and construction in California–performance, constructability, and economics. In: SEAOC 2004 Annual Convention Proceedings; 2004. p. 147–54.
[14] Green RA, Bommer JJ. What is the smallest earthquake magnitude that needs to Be considered in assessing liquefaction hazard? Earthq Spectra 2019;35(3):1441–64.
[15] Green RA, Lee J. "Liquefaction risk mitigation," *deep foundations*. Sept/Oct. Hawthorne, NJ: The Magazine for the Deep Foundations Institute; 2012. p. 47–8.
[16] Green RA, Olgun CG, Wissmann KJ. Shear stress redistribution as a mechanism to mitigate the risk of liquefaction," geotechnical earthquake engineering and soil dynamics IV. In: Zeng David, Manzari Majid T, Hiltunen Dennis R, editors. ASCE Geotechnical Special Publication (GSP) 181; 2008.
[17] Green RA, Maurer BW, van Ballegooy S. The influence of the non-liquefied crust on the severity of surficial liquefaction manifestations: case history from the 2016 valentine's day earthquake in New Zealand," Proc. Geotechnical earthquake engineering and soil dynamics V (GEESD V), liquefaction triggering, consequences, and mitigation. In: Brandenberg SJ, Manzari MT, editors290. ASCE Geotechnical Special Publication (GSP); 2018. p. 21–32.
[18] Green RA, Bommer JJ, Rodriguez-Marek A, Maurer B, Stafford P, Edwards B, Kruiver PP, de Lange G, van Elk J. Assessing the liquefaction hazard in the Groningen region of The Netherlands due to induced seismicity: limitations of existing procedures and development of a Groningen-specific framework. Bull Earthq Eng 2019;17(8):4539–57.
[19] Green RA, Bommer JJ, Stafford PJ, Maurer BW, Kruiver PP, Edwards B, Rodriguez-Marek A, de Lange G, Oates SJ, Storck T, Omidi P, Bourne SJ, van Elk J. Liquefaction hazard in the groningen region of The Netherlands due to induced seismicity. J Geotech Geoenviron Eng 2020;146(8):04020068.
[20] Idriss IM, Boulanger RW. Soil liquefaction during earthquake. Monograph MNO-12. Oakland, CA: Earthquake Engineering Research Institute; 2008.
[21] Ishihara K. Stability of natural deposits during earthquakes. San Francisco, California, USA: *11th International Conference on Soil Mechanics and Foundation Engineering (San Francisco), ISSMGE*; 1985.
[22] Itasca Consulting Group, Inc.. FLAC - fast Lagrangian analysis of continua, Ver.8.0. 2016. Itasca, Minneapolis, MN.
[23] Jamiolkowski M, Ladd CC, Germaine JT, Lancellotta R. New developments in field and laboratory testing of soils. San Francisco, California. Proc 11th int. Conf. On soil mechanics and foundation engineering, 1; 1985. p. 57–153. August 1985.
[24] Kottke AR, Rathje EM. Technical manual for STRATA. Rep. No. 2008/10, pacific earthquake engineering research center. Berkeley, CA: University of California; 2008.
[25] Kramer SL. Geotechnical earthquake engineering. Upper Saddle River, NJ: Prentice Hall; 1996.
[26] Kulhawy FH, Mayne PH. Manual on estimating soil properties for foundation design. Report EL-6800 Electric Power Research Institute, EPRI; 1990.
[27] Lysmer J, Kuhlemeyer RL. Finite dynamic model for infinite media. J Eng Mech 1969;95(EM4):859–77.
[28] Meshkinghalam H, Hajialilue-Bonab M, Khoshravan Azar A. Numerical investigation of stone columns system for liquefaction and settlement diminution potential. Int. J. Geo-Eng. 2017;8(1). Springer Singapore.
[29] Mitchell JK. Soil improvement - state-of-the-art report. Proc. 10th Int. Conf. Soil Mechan. Found. Eng. 1981;4:509–65. Stockholm.
[30] Montgomery J, Ziotopoulou K. Numerical simulations of selected LEAP centrifuge experiments with PM4Sand in FLAC. In: Kutter B, Manzari M, Zeghal M, editors. Model tests and numerical simulations of liquefaction and lateral spreading. Cham: Springer; 2020. https://doi.org/10.1007/978-3-030-22818-7_24.
[31] NRC. State of the art and practice in the assessment of earthquake-induced soil liquefaction and its consequences. Washington, DC: The National Academies Press; 2016. https://doi.org/10.17226/23474.
[32] NZGD. New Zealand geotechnical Database. New Zealand earthquake commission. 2021. Available at: https://www.nzgd.org.nz/. [Accessed 1 January 2021].
[33] Papadimitrious AG, Vytiniotis AC, Bouckovalas GD, Bakas GJ. Equivalence between 2d and 3d numerical simulations of the seismic response of improved sites. In: Proc., 8th U.S. National Conf. on Earthquake Engineering; 2006. Oakland, CA, Earthquake Engineering Research Institute.
[34] PEER. Ground motion Database. www.ngawest2.berkeley.edu/.
[35] Potter SH, Becker JS, Johnston DM, Rossiter KP. An overview of the impacts of the 2010-2011 Canterbury earthquakes. Int. J. Disaster. Risk. Red. 2015;14(1):6–14.
[36] Rahmani A, Baez JI. New approach to determine composite shear wave velocity of improved ground sites. J Geotech Geoenviron Eng 2020;146(10):06020017.
[37] Ramirez J, Petracca M, Dashti S, Liel A. Numerical simulation of nonlinear structures on liquefiable soils with ground improvement. Rome, Italy. 7th international conference on earthquake geotechnical engineering. 2019.

[38] Rayamajhi D, Nguyen TV, Ashford SA, Boulanger RW, Lu J, Elgamal A, Shao L. Numerical study of shear stress distribution for discrete columns in liquefiable soils. J Geotech Geoenviron Eng 2014;140(3):1–9.

[39] Roberts JN. Field evaluation of large-scale, shallow ground improvements to mitigate liquefaction triggering. Ph.D. thesis,. Austin, TX: University of Texas at Austin; 2017.

[40] Robertson PK, Cabal KL. Guide to Cone penetration testing for geotechnical engineering. sixth ed. Gregg Drilling Testing, Inc; 2015.

[41] Saade A. Numerical analysis of rap elements under dynamic loading. M.S. thesis. Blacksburg, VA: Virginia Polytechnic Institute and State University; 2018.

[42] Schaefer VR, Berg RR, Collin JG, Christopher BR, DiMaggio JA, Filz GM, Bruce DA, Ayala D. Ground modification methods reference manual - volume I [FHWA-NHI-16-027]. Geotech. Eng. Circ. No. 2017;13(132034):386. I.

[43] Schroeder WL, Byington M. Experiences with compaction of hydraulic fills. Proc., tenth annual engineering geology and soils engineering symposium). 1972. Moscow, ID.

[44] Seed B, Pyke R, Martin GR. Effect of multi-directional shaking on liquefaction of sands" *rep. No. EERC 75-41 december 1975*, earthquake engineering research center. Berkeley, CA: University of California; 1975.

[45] Shahir H, Pak A, Ayoubi P. A performance-based approach for design of ground densification to mitigate liquefaction. Soil Dynam Earthq Eng 2016;90:381–94.

[46] Shenthan T, Thevanayagam S, Martin GR. Densification of saturated silty soils using composite stone columns for liquefaction mitigation. Proc., 13th world conf. On earthquake engineering. Vancouver, BC: Canada; 2004.

[47] Tiznado JC, Dashti S, Ledezma C, Wham BP, Badanagki M. Performance of embankments on liquefiable soils improved with dense granular columns: observations from case histories and centrifuge experiments. J Geotech Geoenviron Eng 2020;146(9):04020073.

[48] Tonkin, Taylor. "Residential Ground Improvement: Findings from Trials to Manage Liquefaction Vulnerability." Earthquake Commission (EQC). 2015. https://www.eqc.govt.nz/what-we-do/eqc-research-programme/ground- improvement-programme.

[49] Tong B. A study of effectiveness of ground improvement for liquefaction mitigation. Ph.D. thesis. Ames, IA: Iowa State University; 2014.

[50] van Ballegooy S, Cox SC, Thurlow CK, Rutter HK, Reynolds T, Harrington G, Fraser J, Smith T. Median Water Table Elevation in Christchurch and Surrounding Area After the 4 September 2010 Darfield earthquake. GNS Science Report, Institute of Geological and Nuclear Sciences Limited18; 2014.

[51] van Ballegooy S, Roberts JN, Stokoe II KH, Cox BR, Wentz F, Hwang S. Large-scale testing of ground improvements using controlled staged- loading with T-Rex. Proc., 6th international conference on earthquake geotechnical engineering. Christchurch, NZ: ISSMGE; 2015.

[52] Verdugo R, González J. Liquefaction-induced ground damages during the 2010 Chile earthquake. Soil Dynam Earthq Eng 2015;79:280–95.

[53] Wissmann KJ, van Ballegooy S, Metcalfe BC, Dismuke J, Anderson C. Rammed aggregate pier ground improvement as a liquefaction mitigation method in sandy and silty soils. Proc., 6th international conference on earthquake geotechnical engineering. ISSMGE; 2015.

[54] Wotherspoon LM, Orense R, Jacka M, Green RA, Cox BR, Wood C. Seismic performance of improved ground sites during the Canterbury earthquakes. Earthq Spectra 2014;30(1):111–29.

[55] Wotherspoon LM, Orense R, Bradley BA, Cox BR, Wood C, Green RA. Geotechnical Characterization of Christchurch Strong Motion Stations. Project No. 12/629, Earthquake Commission Biennial Grant Report. 2014.

[56] Wotherspoon LM, Cox BR, Stokoe II KH, Ashfield DJ, Phillips RA. Assessment of the degree of soil stiffening from stone column installation using direct push crosshole testing. In: 16th world conference on earthquake. 593; 2017.